

Probing and Controlling Autoionization Dynamics with Attosecond Light Pulses in a Strong Dressing Laser Field

Wei-Chun Chu,^{1,2,*} Toru Morishita,³ and C. D. Lin¹

¹*J. R. Macdonald Laboratory, Department of Physics,
Kansas State University, Manhattan, Kansas 66056, U. S. A.*

²*Max Planck Institute for the Science of Light,
Günther-Scharowsky-Straße 1, 91058 Erlangen, Germany*

³*Department of Engineering Science, The University of Electro-Communications,
1-5-1 Chofu-ga-oka, Chofu-shi, Tokyo, 182-8585, Japan*

(Received September 18, 2013)

We review the theoretical investigations of the autoionizing wave packet excited by an isolated attosecond pulse and dressed by a time-delayed intense laser pulse. The few-level model is described and the applications in photoemission and photoabsorption are given. For the three-level, resonantly coupled system, the main features are explained by the Rabi oscillation modulated in the dressing field. For such a system, by precisely controlling the intensity and the time delay of the dressing pulse, we show the shaping of the attosecond pulse when propagating in a gas medium. A more sophisticated multi-level system with coupling terms involving continuum states is also developed, in which the importance of the continuum-continuum coupling is evaluated with the help of an *ab initio* calculation.

DOI:

PACS numbers: 32.80.Qk, 32.80.Zb, 42.50.Gy

I. INTRODUCTION

Atomic and molecular physics deals with systems in the quantum mechanical spatial and temporal scales. These quantum systems are traditionally studied by energy-domain measurements with highly developed spectroscopic tools. The absolute domination of the energy-domain measurements has changed in the past two decades as the ultrafast tools have acquired better precision, stability, and efficiency over time. One of the most remarkable ultrafast technologies in recent years is the emergence of reliable, table-top light sources in the attosecond timescales in the forms of attosecond pulse trains (APTs) and isolated attosecond pulses (IAPs), which are enabled by the high harmonic generation (HHG) in noble gases [1, 2]. These light sources have now become indispensable tools for the measurement and control of ultrafast electronic dynamics in quantum systems. In this article, we limit ourselves to the use of IAPs for their absolute short timescales and the broadband features, while thorough introductions to the APTs can be found in extensive review articles [3, 4]. Using extreme ultraviolet (XUV) IAPs synchronized with intense infrared (IR) pulses to detect electronic dynamics was demonstrated in 2001 for the first time in the photoelectron emission of krypton atoms [5], and the general method has since been applied to study many

*Electronic address: wei-chun.chu@mpl.mpg.de

atomic and molecular processes, including electron tunneling [6], autoionization [7–10], ac Stark effect [11], and dissociation [12] and ionization [13] of molecules.

Autoionization is a fundamental electron correlation effect in quantum systems. With the typical timescale of a few to a few hundreds of femtoseconds, the excited autoionizing state (AIS) decays to the degenerate background continuum, leaving an asymmetric resonance shape in the photoemission (photoelectron) spectroscopy (PES) or photoabsorption spectroscopy (PAS), which has been characterized by Fano with a simple formula [14]. Physicists have long been observing “Fano resonances” in spectroscopy, most commonly in synchrotron radiations for high precision measurements. The asymmetry and the width of the lineshape are determined by the fraction of the metastable-state quantum pathway and the lifetime of the metastable state, respectively, in a photoionization event. The theory thus connects the spectral measurement to the dynamics of the autoionization process.

Along the development of mode-locked lasers and strong field physics [15], autoionizing systems in strong coupling fields, in analogy to the condition for the electromagnetically induced transparency (EIT) done in bound excited states [16], have been carried out in numerous theoretical reports [17–20] and experiments [21, 22]. The EIT effect has been well established and become the base of a number of modern optical techniques [23] and can readily explain the main features in the coupled autoionizing systems. However, the pulses therein were still considered long compared to the autoionization process and could not resolve the dynamics directly. The direct time-domain measurement of autoionization was infeasible until the recent breakthrough in attosecond light sources and in related ultrafast techniques. For an IAP-excited AIS, the time evolution and the general behavior of the unperturbed wave packet has been treated numerically [24, 25]. In the XUV+IR configuration, by utilizing the IR simply to deplete the AIS or to “streak” [26–28] the photoelectrons, the time-domain studies in autoionization were performed theoretically [29, 30] and experimentally [7, 8], where the AIS lifetimes could be retrieved. However, such studies did not capture the strong coupling between resonances that were emphasized in Refs. [17–22], and thus limited the capability of the dressing field to effectively manipulate the autoionizing system. Beside the models, *ab initio* calculations have also been employed for the time-domain experiments for autoionization [31, 32]; however, they are usually numerically expensive and hard to be extended to more complex systems.

Our goal in this article is to review the development and application of the few-level model which considers the ultrafast coupling between autoionizing states using a synchronized pair of pulses—an IAP and a few-femtosecond intense laser pulse [33–36]. The wave packet evolving in time is simulated, which returns the PES or PAS comparable to experimental measurements. In all scenarios, the ability to control the autoionizing wave packet relies on time-resolving the dynamics of autoionization, the Rabi oscillation, and the evolution of the pulses. The treatment of the continuum states in such an attosecond wave packet needs to go beyond earlier approaches [17–20], which would then trigger spectral features unexpected previously.

The article is organized in the following way. In Sec. II, the EIT-like coupled autoionizing system is presented. The model for the wave packet evolution is described, which provides the fundamentals for spectroscopic calculations. Sec. III introduces the PES in

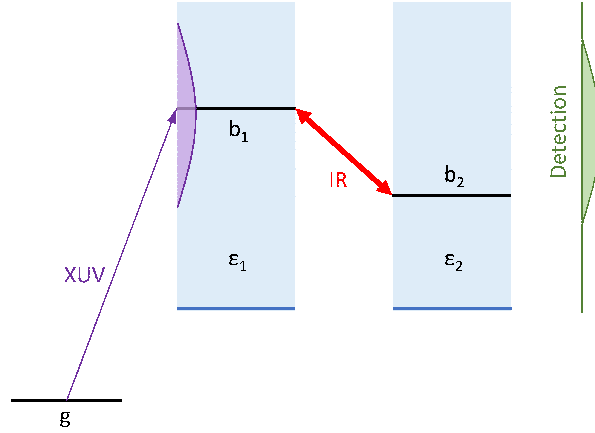


FIG. 1: Schematics of the coupled three-level autoionizing system. The XUV IAP excites the wave packet around the $|b_1\rangle$ - $|\epsilon_1\rangle$ resonance, while the intense IR pulse couples it to the other AIS.

this model and demonstrates an attosecond time-delayed PES of the $2s2p(^1P)$ resonance in helium dressed by a strong laser pulse. In Sec. IV, the simulation for PAS is illustrated and demonstrated in the same system. Comparison is made against the simulation with long pulses, which recovers the typical EIT features. In Sec. V, propagation of the IAP is then considered for the realistic pulse reshaping. A remarkable enhanced resonant part of the IAP was theoretically predicted. While the above sections deal with the three-level system, Sec. VI extends the model to include multiple AISs and the coupling involving continuum states, with the help by the *ab initio* calculation. The retrieval of the atomic structure is shown possible in the presence of such coupling terms. In all sections, for the model description, atomic units (a.u.) are used unless otherwise specified, and for applications, electron Volts (eV) are used for energy and femtoseconds (fs) are used for time unless otherwise specified.

II. THREE-LEVEL WAVEFUNCTION

Three-level systems coupled by laser fields are most notably studied for coherent population trapping (CPT) [37, 38] and the EIT effect [16, 23]. It is common to solve the time-dependent Schrödinger equation (TDSE) for the coherent quantum state of the system in terms of the atomic eigenstates. With intense laser pulses, as what this article concerns, the field is treated classically. Our intention is to calculate the time-evolution of the wavefunction for the Hamiltonian of the system specified by a given set of atomic parameters and the external field.

For coupled AISs, as differing from coupled bound states, the continuum states associated to the AISs are included in the total wavefunction as in Refs. [17–20] and illustrated in Fig. 1. The wavefunction can be generally written in the form of

$$\begin{aligned}
|\Psi(t)\rangle = & e^{-i\epsilon_g t} c_g(t) |g\rangle + e^{-i\epsilon_e t} \left[c_{b_1}(t) |b_1\rangle + c_{b_2}(t) |b_2\rangle \right. \\
& \left. + \int c_{\epsilon_1}(t) |\epsilon_1\rangle d\epsilon_1 + \int c_{\epsilon_2}(t) |\epsilon_2\rangle d\epsilon_2 \right], \tag{1}
\end{aligned}$$

where $|g\rangle$ is the ground state, $|b_1\rangle$ and $|b_2\rangle$ are the bound configurations of the two Fano resonances, and $|\epsilon_1\rangle$ and $|\epsilon_2\rangle$ are the two groups of continuum states associated with $|b_1\rangle$ and $|b_2\rangle$, respectively. The energy levels of the three bound states are ϵ_g , ϵ_{b_1} , and ϵ_{b_2} , respectively, and $\epsilon_e \equiv \epsilon_g + \omega_X$ is the central energy of the excited wave packet, with the XUV central frequency ω_X factored out of the excited wave packet. Note that the $|b\rangle$ and $|\epsilon\rangle$ states are not eigenstates of the atomic system, but rather a convenient choice where autoionization can be visualized. With the XUV+IR setup, the $|b_1\rangle$ - $|\epsilon_1\rangle$ resonance is directly excited by the XUV from the ground state, when the $|b_1\rangle$ and $|b_2\rangle$ AISs are coupled by the IR field. The coupling scheme is plotted in Fig. 1 schematically. The XUV field is expressed in the envelope form as $E_X(t) = F_X(t)e^{i\omega_X t} + F_X^*(t)e^{-i\omega_X t}$, but the IR field $E_L(t)$ is kept in its numerical form because it may be a few-cycle pulse. The XUV envelope $F_X(t)$ is a smooth function of time against the fast oscillation with the carrier frequency ω_X . It is in general complex and it contains any extra phase additional to the carrier phase.

Taking only the electric dipole terms in the light-matter interaction, the Hamiltonian of the system is written as

$$H(t) = H_A - D \cdot E(t), \tag{2}$$

where H_A is the atomic Hamiltonian determined by the field-free atomic structure, D is the dipole operator, and $E(t)$ is the total external field. The off-diagonal terms of H_A in the current basis, $V_{b_1\epsilon_1} = \langle b_1 | H_A | \epsilon_1 \rangle$ and $V_{b_2\epsilon_2} = \langle b_2 | H_A | \epsilon_2 \rangle$, are responsible for the autoionization. By solving TDSE with this Hamiltonian, the coupled equations for the coefficients in Eq. (1) are obtained. For the system in concern, the following representations and approximations are then made to simplify the model: (1) Standing wave representation is taken for the basis set, so all the matrix elements in the Hamiltonian are real. The use of such basis is conventional and does not impose any physical restriction. (2) The AISs are assumed to be far above the ionization threshold compared with their widths, where the scattered electrons have almost constant momentum across the AISs. As a consequence, the atomic parameters can be viewed as constants estimated at the resonance frequencies, i.e., $V_{b_1\epsilon_1} = V_{b_1\epsilon_{b_1}} \equiv V_{b_1}$, $D_{g\epsilon_1} = D_{g\epsilon_{b_1}} \equiv D_{g1}$, and so on. This approximation is good in many autoionizing systems; for example, the $2s2p(^1P)$ resonance in helium is 35 eV above the binding energy compared to its width of 37 meV. (3) Rotating wave approximation is applied to the XUV since its photon energy is roughly on resonance with the AISs within a confined bandwidth. (4) By assuming that the continuum state coefficients evolve slowly in time, we employ adiabatic elimination (AE) for them. With these assumptions, we arrive at the self-contained equation of motion (EOM) for the bound part of the wavefunction,

given by

$$i\dot{c}_g(t) = -F_X(t)\bar{D}_{gb_1}c_{b_1}(t) - i|F_X(t)|^2 j_{gg}c_g(t), \quad (3)$$

$$i\dot{c}_{b_1}(t) = -F_X^*(t)\bar{D}_{gb_1}c_g(t) - (\delta_1 + i\kappa_1)c_{b_1}(t) - E_L(t)D_{b_1b_2}c_{b_2}(t), \quad (4)$$

$$i\dot{c}_{b_2}(t) = -(\delta_2 + i\kappa_2)c_{b_2}(t) - E_L(t)D_{b_1b_2}c_{b_1}(t), \quad (5)$$

where $j_{gg} \equiv \pi|D_{g1}|^2$ is the broadening of the ground state by the field, $\delta_1 \equiv \epsilon_e - \epsilon_{b_1}$ and $\delta_2 \equiv \epsilon_e - \epsilon_{b_2}$ are the detuning of the XUV to the AISs, $\Gamma_{b_1} = 2\kappa_{b_1} \equiv 2\pi|V_{b_1}|^2$ and $\Gamma_{b_2} = 2\kappa_{b_2} \equiv 2\pi|V_{b_2}|^2$ are the resonance widths, and $\bar{D}_{gb_1} \equiv D_{gb_1} - i\pi V_{b_1}D_{g1}$ is the composite dipole matrix element between $|g\rangle$ and $|b_1\rangle$ consisting the direct and indirect paths. Note that \bar{D}_{gb_1} is complex although the individual dipole matrix elements are real in the standing wave representation. The Fano lineshape parameter $q \equiv D_{gb_1}/(i\pi V_{b_1}D_{g1})$ is determined exclusively by the atomic structure parameters D and V and already embedded in the coupled equations. The bound part of the wavefunction is carried out without any numerical treatment for the continuum coefficients. The required input parameters are the V and D values which are totally determined by the atomic structure, and the external field parameters. Up to this point, the model can deal with problems with long pulses where their narrow bandwidths are viewed as energy points in the spectrum, and the wave packet has negligible portion of the continuum states, as shown in Refs. [17–22].

With the use of ultrashort pulses, when the pulse length gets comparable to or even shorter than the autoionization, the bandwidth covers an energy range comparable to or wider than the resonance width. This means that the short pulse excites a considerable portion of the continuum states around the AISs, and the evolving wave packet has to include the continuum part. To this end, the continuum state coefficients are calculated by bringing in the original coupled equations,

$$i\dot{c}_{\epsilon_1}(t) = (\epsilon_1 - \epsilon_g - \omega_X)c_{\epsilon_1}(t) + V_1c_{b_1}(t) - F_X^*(t)D_{g1}c_g(t), \quad (6)$$

$$i\dot{c}_{\epsilon_2}(t) = (\epsilon_2 - \epsilon_g - \omega_X)c_{\epsilon_2}(t) + V_2c_{b_2}(t), \quad (7)$$

where all the bound state coefficients therein have already been solved in Eqs. (3)-(5). The recovery of the continuum state coefficients is an iteration process which ‘‘corrects’’ the zeroth order solution that is only used in the AE. Note that the solution at each energy point in Eqs. (6) and (7) is independent of other energy points, so the precision of the solution is irrelevant to the energy range and the energy resolution taken in the computation. Up to here the total wave function of this atomic system is calculated, where all observables can be derived accordingly.

III. PHOTOEMISSION

For photoionization events, PES, PAS, and photoion spectroscopy are all common measurements. In PES, with various detection angles against the polarization direction, the scattered electrons in momentum space are recorded. Let the excited part of the wave packet in Eq. (1) be denoted by $|\Psi_E(t)\rangle$. The momentum distribution of the detected

scattered electrons can then be written as $P(\vec{k}) = \left| \langle \psi_{\vec{k}}^{(-)} | \Psi_E(t_f) \rangle \right|^2$, where $P(\vec{k})$ is the probability density in the momentum space, $|\psi_{\vec{k}}^{(-)}\rangle$ is the momentum eigenstate with the incoming boundary conditions, and t_f is the time of the detection, which should be very large in the atomic timescale. The momentum eigenstates can be written in the coordinate space as the expansion of the scattering partial waves, in the energy-normalized form of

$$\psi_{\vec{k}}(\vec{r}) = \sqrt{\frac{2}{\pi k}} \frac{1}{r} \sum_{lm} i^l e^{-im} u_l(kr) Y_l^m(\hat{r}) Y_l^{m*}(\hat{k}), \quad (8)$$

where $u_l(kr)$ are the radial waves and Y_l^m are the spherical harmonics of angular momentum l and magnetic quantum number m . By removing the azimuth dependence, $P(\vec{k})$ is given in spherical coordinate by

$$P(\epsilon, \theta) = \left| \sum_l \sqrt{\frac{2l+1}{4\pi}} \frac{e^{im}}{i^l} c_{el}(t_f) P_l(\cos\theta) \right|^2, \quad (9)$$

where $\epsilon = k^2/2$ is the kinetic energy, θ is the polar angle with regard to polarization, $c_{el}(t_f)$ are the final continuum state coefficients, and $P_l(\cos\theta)$ are Legendre polynomials.

In the three-level autoionizing system, the two resonances dominate two different partial waves, and their energy spectra can be simulated separately. An angular-integrated spectrum is given by $P(\epsilon) = \sum_l |c_{el}(t_f)|^2$ where $c_{el}(t)$ is the corresponding continuum state coefficients simulated as described in Sec. II. In principle, t_f should be infinitely large when all the dynamic processes are over. Practically, it is set after the external fields and must be much larger than the decay lifetimes of the AISs, since the decay processes are exponential without a definite end. For example, the $2s2p(^1P)$ AIS in helium has a lifetime of 17 fs, and t_f can be set 200 fs later than the end of the external field, at which time the wave packet is finalized in the energy or momentum space [25]. For systems of longer decay lifetimes, a technique to reduce the total calculation time is to project the wave packet right after the end of the external field onto the atomic eigenstates, at which point the eigenstate coefficients will not change anymore (except the regular phase rotation). This technique is based on Fano's configuration theory for autoionization [14] and was described in details in Ref. [33].

For demonstration, we simulate the PES of the $2s2p(^1P)$ resonance (referred as $2s2p$ hereafter) of helium where the "IR" pulse couples this resonance to the $2s^2(^1S)$ resonance (referred as $2s^2$ hereafter). The 500 as XUV is weak and centered at $2s2p$, which linearly excites a broadband autoionizing wave packet. It is much shorter than the 17-fs decay lifetime of $2s2p$ and instantaneously initiates the autoionizing wave packet. The coupling laser pulse (wavelength is 540 nm, pulse length is 7 fs in FWHM, peak intensity is 1.5×10^{12} W/cm²) is actually in the visible wavelength in order to resonantly couple the two AISs. The time-delayed PES is plotted in Fig. 2. The time delay t_0 is defined positive if the XUV comes before the IR. In the spectrogram [Fig. 2(a)], the lineshape remains the same for $t_0 < 0$, but suddenly flips its shape from left to right when t_0 increases to around 6 fs.

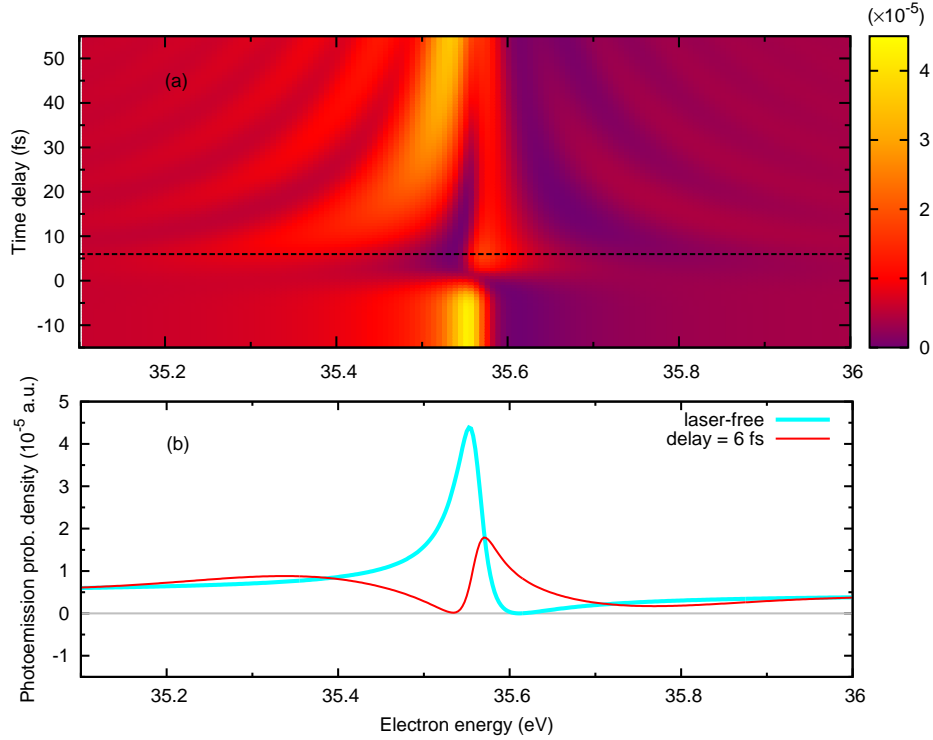


FIG. 2: Time-delayed PES at the $2s2p$ resonance. (a) Spectrogram for time delays between -15 to 55 fs. (b) PES at $t_0 = 6$ fs which displays a horizontally inverse image of the original Fano lineshape additional to an overall reduction. The corresponding time delay is indicated in (a) by the dashed black line. The original lineshape in the laser-free condition is shown in the background for comparison.

When t_0 further increases and becomes large compared to the 17 fs lifetime of $2s2p$, the resonance gradually returns to the original lineshape. The dramatic flipping at 6 fs can be understood by the Rabi oscillation between the two AISs. At $t_0 = 6$ fs, the total dressing field after the XUV pulse has a pulse area of 2π , which means once $2s2p$ is pumped by the XUV, the electrons therein go through one Rabi cycle through $2s^2$ and back to $2s2p$, where the phase of this oscillating part in the wave packet changes by π . This phase shift has the same effect of changing the sign of q and making a mirror image of the lineshape. At the same time, the signal strength drops because for such an autoionizing system, the excited states decay to the continuum all the time, and the population is lost during the Rabi oscillation. The PES for the $2s^2(^1S)$ resonance versus the time delay, which we do not show here, also supports this conclusion [33]. The simulated result by this model compared to a recent measurement [8] has been reported [33].

IV. PHOTOABSORPTION

In the same XUV+IR coupling system, the measurement can also be made in PAS. Attosecond transient absorption (ATA) [39] has been one of the most rapidly developing fields in ultrafast optics. Other than the instrumental concerns and the experimental setup, there are some advantages of the PAS over the PES measurements, such as the access to both the ionized and the neutral species, and the higher energy resolution in spectrometers up to 20 meV at 60 eV as demonstrated in the recent experiment [10]. In measuring autoionizing systems, the lineshape observed in high precision for different time delays would be especially informative of the wave packet dynamics.

In the following we introduce the calculation of PAS based on a given external field and the induced total electronic dipole. The response function $S(\omega)$ is defined as the probability density of the energy that the atomic system absorbs from the field [40]:

$$\Delta U = \int_0^\infty \omega S(\omega) d\omega, \quad (10)$$

where ΔU is the total energy transferred from the field to the atomic system. Following the Hamiltonian in Eq. (2), $S(\omega)$ is given by

$$S(\omega) = -2\text{Im} \left[\tilde{D}(\omega) \tilde{E}^*(\omega) \right], \quad (11)$$

where $D(t)$ is the total electric dipole moment of the atomic system, and the Fourier transform is defined by $\tilde{f}(\omega) = \frac{1}{\sqrt{2\pi}} \int e^{-i\omega t} f(t) dt$. The response function has the same dimensionality of the PES probability density $P(\epsilon)$ presented in Sec. III. Both $S(\omega)$ and $P(\epsilon)$ display the spectral lineshapes of Fano resonances.

For the autoionizing system described by in Eq. (1), the dipole moment $D(t)$ is given by

$$D(t) = e^{i\omega_X t} u_X(t) + u_L(t) + \text{c.c.}, \quad (12)$$

where the XUV and IR frequency components are separate and given by

$$u_X(t) = D_{gb_1} \lambda^* c_{b_1}^*(t) c_g(t) - i F_X(t) j_{gg} |c_g(t)|^2, \quad (13)$$

$$u_L(t) = D_{b_1 b_2} c_{b_2}^*(t) c_{b_1}(t). \quad (14)$$

Because of the separation of the XUV and the IR frequency components in Eq. (12), the PAS can be simulated for only the XUV or IR part of the spectrum. In the current XUV+IR scheme, the IR interacts only with the top two levels, while the overall excitation of these levels is limited by the XUV intensity that is much weaker than the IR. As a consequence, the absorption of IR is negligible compared with the IR pump in most cases in the sense of pulse shaping, unless a very optically thick medium is present. The IR absorption in such a scheme is discussed in Ref. [34], while we deal with only the XUV absorption here. The

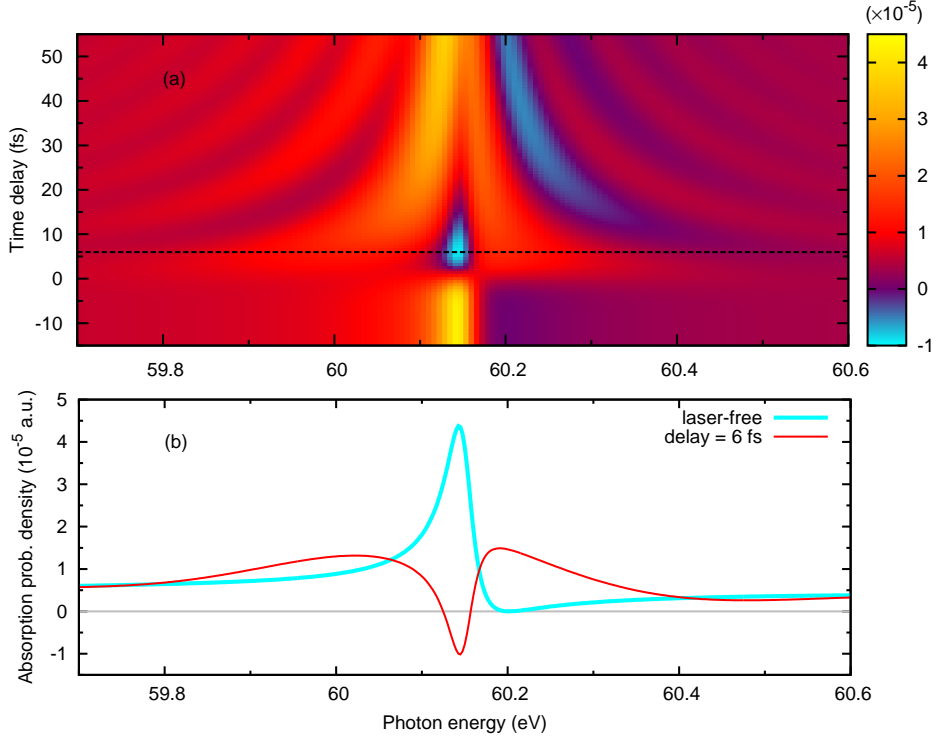


FIG. 3: Same as Fig. 2 but for PAS. The cyan color in (a) indicates the negative absorption, or emission, induced by the dressing field. In (b), the spectrum at $t_0 = 6$ fs shows an upside-down image to the original Fano lineshape in the laser-free condition. Note that the peak of the Fano profile is turned to an emission line by the dressing laser.

response function has a straightforward connection to the commonly used absorption cross section, given by

$$\sigma(\omega) = \frac{4\pi\alpha\omega S(\omega)}{|\tilde{E}(\omega)|^2}, \quad (15)$$

for the linear cases before the propagation effect comes in.

In Fig. 3 we show the simulated response function in the PAS result, for the same system introduced in Sec. III. The spectra in Fig. 3 and Fig. 2 have the same dimensionality and can be directly compared to each other. As seen in the figure, the overall dependence on the time delay is almost the same as the PES result, except that there are some negative signals at $t_0 = 6$ fs at the resonance and in the fringes at larger delays above the resonance energy. These negative values represent the emission of the XUV, which cannot be found in typical EIT measurements. This extraordinary phenomenon can again be explained by the Rabi oscillation as in the PES case. The original Fano lineshape represents the interference between the dipole stored in the continuum electrons and the dipole stored in the bound

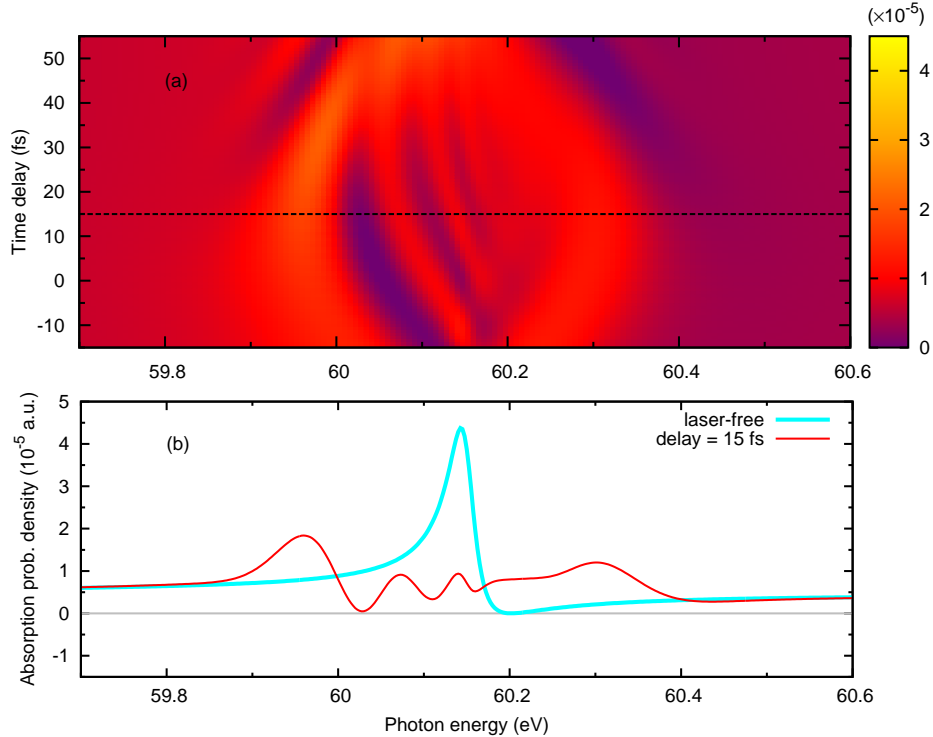


FIG. 4: Same as Fig. 3 but for the longer (50 fs) dressing field. The spectrum at $t_0 = 15$ fs is shown in (b) where the Autler-Townes splitting is the largest.

electrons. At $t_0 = 6$ fs, as the bound electrons go through the $2s2p$ - $2s^2$ - $2s2p$ Rabi cycle, they gain an additional π phase shift. It means that between the two interfering paths, only the bound but not the continuum path changes. The field generated by the coherent sum of the two dipole components, with one of them shifted phase by π , carries the spectral pattern where the constructive and destructive parts of the interference swap. This results in the upside-down lineshape and forms an emission peak at the resonance energy.

In order to elucidate how such an ultrafast three-level coupling differs from the typical EIT system, we conduct an additional simulation with a 50-fs long dressing field. The pulse length is considerably longer than the 17-fs decay lifetime of $2s2p$. Fig. 4 shows the time-delayed PAS of the XUV in this dressing field. The most obvious feature in the spectrogram is the splitting of the absorption peak, whose separation distance changes with the time delay. The separation reaches maximum at $t_0 = 15$ fs as shown in Fig. 4(b). The separation there of about 3.5 eV is the same as the Rabi frequency of the dressing field, which is expected as the Autler-Townes doublet [41] in such an EIT scheme. As the dressing pulse temporally shifts away from the XUV, the absorption profile returns to the single-peak shape. It suggests that the whole XUV-excited wave packet “sees” a stable dressing field most strongly at $t_0 = 15$ fs, when the existence of the $2s2p$ within its lifetime is mainly at the peak of the dressing pulse. This type of adiabatic control utilizes the time delay

between the XUV and the IR to turn on or turn off the EIT effect and has been carried out experimentally in Ref. [22].

V. PROPAGATION EFFECT

The linear absorption of light across a gas medium can be described by Beer's law [42], i.e.,

$$T(\omega) = T_0(\omega) \exp[-\rho L \sigma(\omega)], \quad (16)$$

where $T_0(\omega)$ and $T(\omega)$ are transmission spectra before and after the gas medium of number density ρ and propagation length L . The absorption cross section $\sigma(\omega)$ represents the rate of absorption which does not change along the path of light. On the contrary, in the nonlinear regime, the absorption is strongly dependent on the instantaneous electric field, and the cross section evolves over the distance where the light pulse reshapes itself. In such cases, Maxwell equation has to be applied.

Similar to the consideration in Sec. IV, we focus on the propagation of the XUV where the IR is assumed to propagate without change across the medium. Applying loosely focusing condition which is typical in ATA spectroscopy, we assume that the electric field is transverse to the pulse propagation in the forward z direction. Using the coordinate transformation $t' = t - z/c$, the Maxwell equation can be simplified to the first-order form of

$$\frac{\partial E(z, t')}{\partial z} = -\frac{\rho}{2c\epsilon_0} \frac{\partial D(z, t')}{\partial t'}. \quad (17)$$

At each spatial point, the total wavefunction and the dipole oscillation in time is calculated in the given external field, which then determines the field at the next point, from the front to the rear end of the medium. Taking only the XUV field into account, the envelope of the XUV is propagated by

$$\frac{\partial F_X(z, t')}{\partial z} = -\frac{\rho}{2c\epsilon_0} \left[\frac{\partial u_X(z, t')}{\partial t'} + i\omega_X u_X(z, t') \right], \quad (18)$$

where $u_X(t)$ represents the envelope of the XUV dipole, given in Eq. (13).

In Sec. IV, the emission peak of the XUV is induced by a precisely controlled dressing-field. It is shown as the negative absorption in the response function, or equivalently, in the single-atom absorption cross section. However, a negative absorption rate cannot sustain itself physically in an actual medium, or it would become singular at certain spatial point. Thus, it is interesting to simulate this emission peak and to study its behavior in the medium with actual propagation effects. With the same helium system and the same field parameters in Sec. III, we assume a gas medium of the pressure of 25 Torr at room temperature, which is equivalent to the number density of $8 \times 10^{17} \text{ cm}^{-3}$. Simulation carried out up to the propagation distance of $z = 2 \text{ mm}$ is shown in Fig. 5, where the general trend

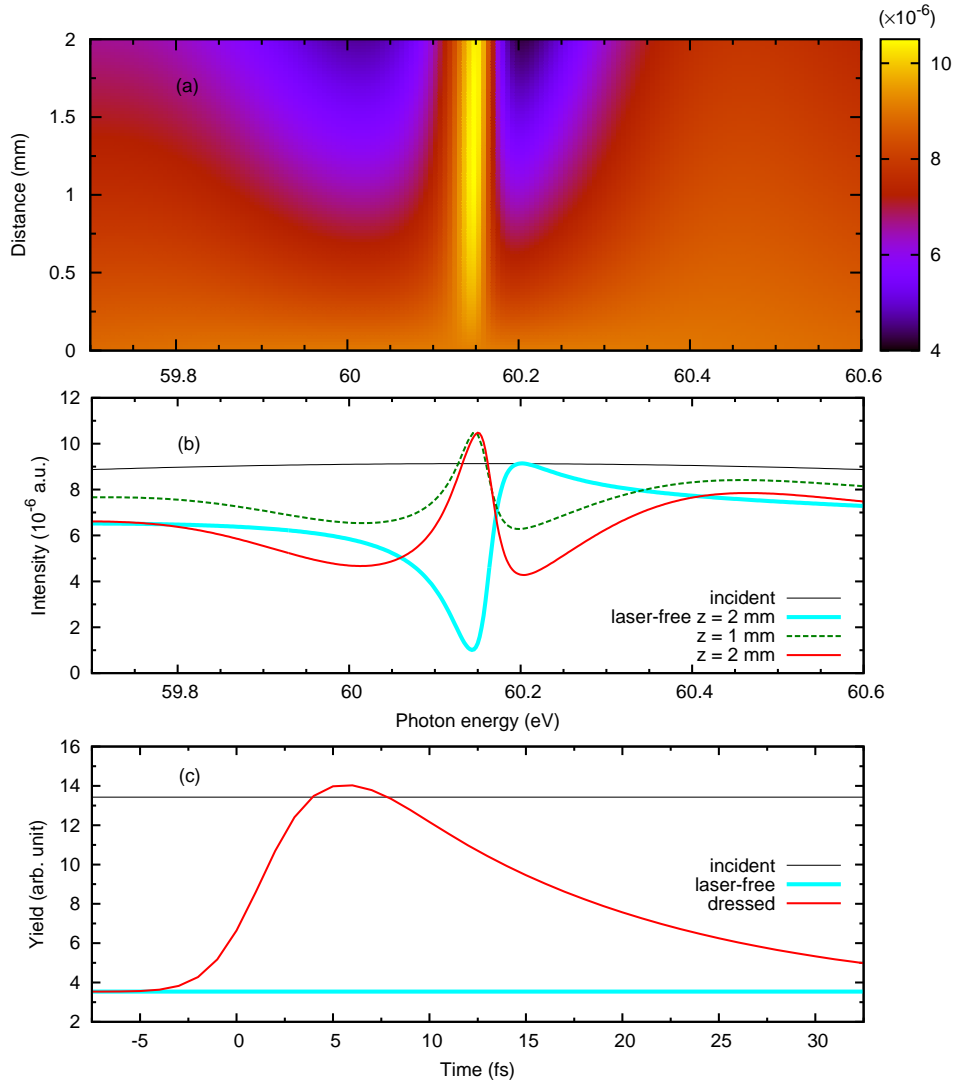


FIG. 5: Transmission spectra along the propagation distance in the medium for $t_0 = 6$ fs and the same field parameters used previously. (a) The propagation from $z = 0$ to 2 mm. (b) The spectra at $z = 1$ and 2 mm. The emission peak persists in the propagation while the surrounding signal decreases over the distance. The Fano lineshape produced at 2 mm in the laser-free case is plotted as a reference. (c) The total transmitted signal within a 40 meV interval at the resonance energy at $z = 2$ mm versus the time delay.

along the path and the detail spectral shapes at 1 and 2 mm are shown in Fig. 5(a) and Fig. 5(b), respectively. It shows that in contrast to the Beer's law, the emission part of the propagating spectrum does not (and cannot) grow exponentially. Instead, it remains the height along the propagation, while the background signal around it drops exponentially, as clearly seen by the $z = 1$ and 2 mm spectra in Fig. 5(b). This remarkable case exemplifies

the redistribution of the XUV photons controlled by the IR dressing pulse, while the total XUV energy attenuates along the propagation in the medium regardless of the appearance of the IR.

As shown in Fig. 3, in the single-atom calculation, a strong modulation of the emission peak lies on the time delay of the laser pulse. In the macroscopic simulation here, in order to emphasize this modulation at the resonance, we assume a spectrometer with the energy resolution of $\Delta\epsilon = 40$ meV at the resonance position at 60.15 eV. By collecting the transmitted XUV within this $\Delta\epsilon$ interval, the total yield at the exit of the medium ($z = 2$ mm) is plotted against the time delay in Fig. 5(c). As predicted by the single-atom case, the strongest emission occurs at $t_0 = 6$ fs, which is clearly higher than the incident light, i.e., the XUV experiences a gain at the resonance frequency in the medium. As the time delay moves away from this optimal value, the XUV starts to be absorbed. With large temporal separation between the pulses, the level of absorption rises back to that of the original Fano lineshape. The variation of the emission yield along the time delay, specified by the 40-meV spectral window, shows a strong manipulation on a broadband attosecond pulse, in both the energy domain and the time domain. Further discussions and demonstrations for the intensity dependence is given in Ref. [35].

VI. CONTINUUM-CONTINUUM COUPLING

The IR coupling in the model illustrated in Fig. 1 is between the bound states for taking only the first-order transition, where the coupling involving any continuum state is neglected. However, if we widen the bandwidth of an ultrashort coupling pulse that covers a continuum with a number of embedded bound states, the collective transition to the continuum will increase, but the transition to the bound states will stay the same since it is already confined by the resonances' own widths. Consequently, neglecting the coupling through continuum states, i.e., bound-continuum coupling and continuum-continuum (C-C) coupling, is not appropriate once the pulse becomes shorter. To bring such coupling into the model and to test its validity, we employ an *ab initio* two-active-electron (TAE) TDSE calculation [43, 44] as a virtual experiment to calibrate the model. The TAE-TDSE method describes the time evolution of the two-electron wavefunction in space in the nuclear potential. It then projects the total wavefunction onto the eigenstate wavefunctions with the correct scattering boundary conditions to obtain the energy spectrum for each partial wave. To conduct a realistic calibration for the model, the size of the system in Sec.II is further expanded so that each symmetry in the coupling possesses multiple AISs. The coupling scheme is plotted in Fig. 6.

The total wavefunction of the system in Fig. 6 is given by

$$\begin{aligned}
 |\Psi(t)\rangle = & e^{-i\epsilon_g t} c_g(t) |g\rangle + e^{-i\epsilon_e t} \left[\sum_m c_m(t) |m\rangle + \sum_n c_n(t) |n\rangle \right. \\
 & \left. + \int c_{\epsilon_1}(t) |\epsilon_1\rangle d\epsilon_1 + \int c_{\epsilon_2}(t) |\epsilon_2\rangle d\epsilon_2 \right].
 \end{aligned} \tag{19}$$

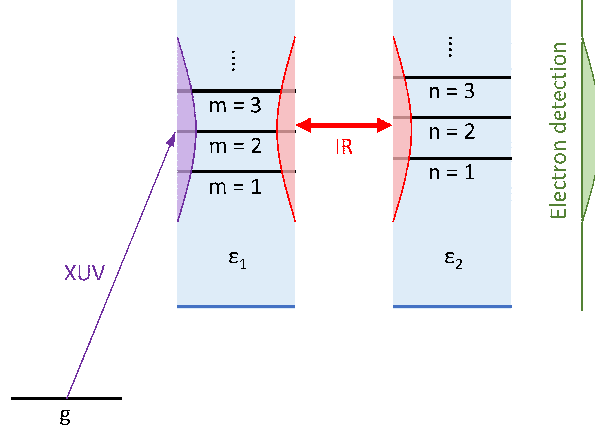


FIG. 6: Schematics of the IR coupling between two groups of Fano resonances that are excited by a XUV IAP. Both the bound and the continuum parts of the resonances are coupled by the IR.

To simplify the calibration with the TAE-TDSE, we limit the XUV intensity to avoid second-order excitation. In such a condition, the ground state coefficient $c_g(t) = 1$ is a constant of time. By taking into account all the dipole matrix elements including the ones involving continuum states and applying AE for the continuum, the coupled equations for the bound states are

$$i\dot{c}_m(t) = -F_X^*(t)\bar{D}_{gm} - (\delta_m + i\kappa_m)c_m(t) - E_L(t)\sum_n \bar{D}_{mn}c_n(t), \quad (20)$$

$$i\dot{c}_n(t) = -iF_X^*(t)E_L(t)j_{gn} - (\delta_n + i\kappa_n)c_n(t) - E_L(t)\sum_m \bar{D}_{mn}c_m(t), \quad (21)$$

where

$$\bar{D}_{gm} \equiv D_{gm} - i\pi D_{g\epsilon_m} V_m, \quad (22)$$

$$\bar{D}_{mn} \equiv D_{mn} - \pi^2 V_m D_{\epsilon_m \epsilon_n} V_n - i\pi(V_m D_{\epsilon_m n} + D_{m\epsilon_n} V_n) \quad (23)$$

are the complex composite dipole matrix elements incorporating the continuum states. All the atomic structure parameters in Eqs. (20)-(23) are labelled in the same way as in the three-level system in Sec. II but with the $|m\rangle$ and $|n\rangle$ states replacing $|b_1\rangle$ and $|b_2\rangle$ respectively. One can see that the IR coupling with the continuum states comes into the terms of $D_{\epsilon_m \epsilon_n}$, $D_{\epsilon_m n}$, and $D_{m\epsilon_n}$ in Eqs. (22) and (23) and thus contributing to Eqs. (20) and (21).

To retrieve the continuum state coefficients by iteration, all continuous dipole matrix elements have to be kept in the original coupled equation. With mutual coupling terms between the two background continua, the final continuum state coupled equations are

given by

$$i\dot{c}_{\epsilon_1}(t) = -F_X^*(t)D_{g\epsilon_e} - \delta_{\epsilon_1}c_{\epsilon_1}(t) + \sum_m V_m c_m(t) - E_L(t) \left[\sum_n \bar{D}_{\epsilon_1 n} c_n(t) + \alpha_{\epsilon_1}(t) \right], \quad (24)$$

$$i\dot{c}_{\epsilon_2}(t) = -iF_X^*(t)E_L(t)j_{g\epsilon_2} - \delta_{\epsilon_2}c_{\epsilon_2}(t) + \sum_n V_n c_n(t) - E_L(t) \left[\sum_m \bar{D}_{m\epsilon_2} c_m(t) + \alpha_{\epsilon_2}(t) \right], \quad (25)$$

where

$$\bar{D}_{\epsilon_1 n} \equiv D_{\epsilon_1 n} - i\pi D_{\epsilon_1 \epsilon_n} V_n, \quad (26)$$

$$\bar{D}_{m\epsilon_2} \equiv D_{m\epsilon_2} - i\pi V_m D_{\epsilon_m \epsilon_2}, \quad (27)$$

$$\alpha_{\epsilon_1}(t) \equiv \pi D_{\epsilon_1 \epsilon_2} \dot{c}_{\epsilon_2}(t)|_{\epsilon_2=\epsilon_e}, \quad (28)$$

$$\alpha_{\epsilon_2}(t) \equiv \pi D_{\epsilon_1 \epsilon_2} \dot{c}_{\epsilon_1}(t)|_{\epsilon_1=\epsilon_e}. \quad (29)$$

For each value of ϵ_1 , the evolution of $c_{\epsilon_1}(t)$ has the coupling term of $c_{\epsilon_2}(t)$ only at $\epsilon_2 = \epsilon_e$, which means all the ϵ_2 continuum states together have a collective effect approximated by $\alpha_{\epsilon_1}(t)$, and the same applies to $c_{\epsilon_2}(t)$ too. The α functions are evaluated by Eqs. (28) and (29) with the $c(t)$ coefficients calculated by Eqs. (24) and (25) without the α functions themselves, i.e., they are added iteratively. These terms minimize the numerical burden and consider the C-C coupling at the same time. With the complete wavefunction, the PES for the two continua are $P_1(\epsilon) = |c_{\epsilon_1}(t_f)|^2$ and $P_2(\epsilon) = |c_{\epsilon_2}(t_f)|^2$ as explained in Sec. III.

In the following we take the same example system, the $2s2p$ resonance in helium, for demonstration. The TAE-TDSE calculation is taken as a virtual experiment to calibrate the present model. With the XUV (central frequency is resonant with $2s2p$, FWHM pulse length is 690 fs, peak intensity is 10^9 W/cm²) and the laser (wavelength is 540 nm, FWHM pulse length is 4 fs, peak intensity is 5×10^{11} W/cm²) pulses, both with zero carrier-envelope phase, the TAE-TDSE result shows the first three partial waves— s , p , and d —are the dominant ones in the PES. Thus, in the model, a third continuum is added alongside Eqs. (24) and (25), and all the atomic parameters are adjusted to fit the PES by TAE-TDSE. In Fig. 7, the three dominant partial waves for zero delay between the two pulses are shown in the PES, which achieve a good agreement between the two calculations. The original Fano lineshape, displayed as a reference, is calculated as the p -wave PES in the laser-free condition. With the laser turned on, the strength of the p wave drops down, while both the s and d waves rise up, showing the laser transition from the $2s2p$ resonance and its background to other symmetries. The two s -wave resonances, identified as $2s^2$ and $2p^2(^1S)$ (referred as $2p^2$ hereafter), are well reproduced by the model. Certain signal depletion appears in the model relative to the TAE-TDSE calculation as the result of the laser ionization, which is not considered by the model due to the lack of reliable treatment for strong-field ionization so far.

In Fig. 7, the s -wave PES has a flat signal strength between $2s^2$ and $2p^2$. Considering the laser bandwidth of about 1 eV counted after the XUV excitation, the middle part of this

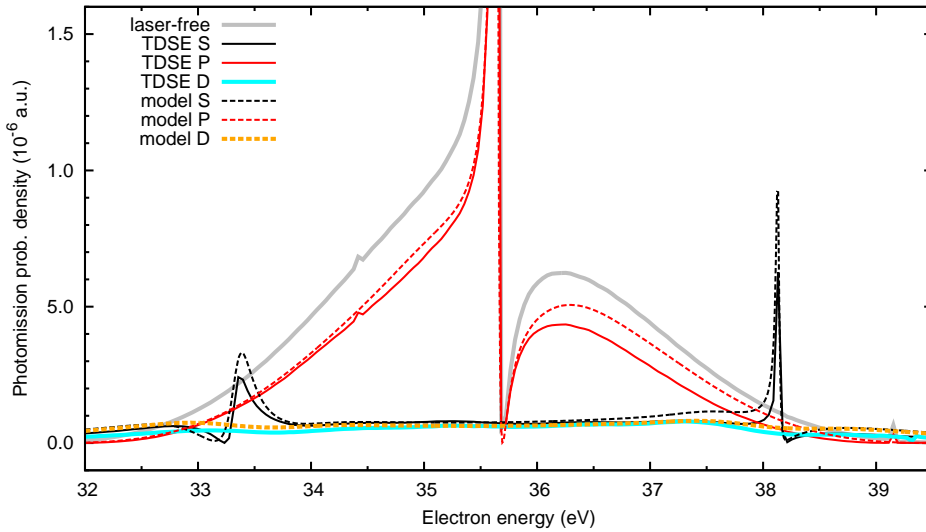


FIG. 7: PES for the s , p , and d partial waves for overlapping XUV and laser pulses ($t_0 = 0$) calculated by TAE-TDSE and the present model. The p wave in the laser-free condition calculated by TAE-TDSE is also plotted as the original Fano lineshape.

flat signal must be the contribution by the C-C transition from the background parts of the p wave. To draw a detail account of the C-C coupling, we plot the s -wave PES with various time delays in Fig. 8. At $t_0 = 0$, the XUV is on top of the maximum field of the laser. As seen in the figure, once the laser lags behind the XUV, as shown at $t_0 = 0.3$ fs, the signal between $2s^2$ and $2p^2$ decreases significantly to about half of its original strength. As the laser lags more, the signal further decreases, but the speed slows down, until at $t_0 = 0.5$ fs the signal drops to nearly zero. Meanwhile, the $2s^2$ and $2p^2$ resonance peaks stay strong and are just slightly changed by the time delay. This contrast between the background and resonance parts of the signal suggests that the C-C coupling by the laser only happens at the beginning of the XUV excitation. Once the autoionizing wave packet is formed by the XUV excitation, the bound state electrons and the photoelectrons are all spatially near the atomic core. The photoelectrons, represented by the continuum states, can thus be coupled by the laser and transferred to other symmetries at this moment. However, if the XUV overlaps the zero field of the laser, the photoelectrons are scattered far away from the core and free from the laser coupling. In principle these “free” electrons are still controlled by the laser through streaking, but in the current case the intensity is low enough to neglect streaking. This observation supports the claim that the C-C coupling is important in a very short period after such a broadband wave packet is formed, which contradicts the common assumption that the C-C coupling is negligible in laser-coupled systems.

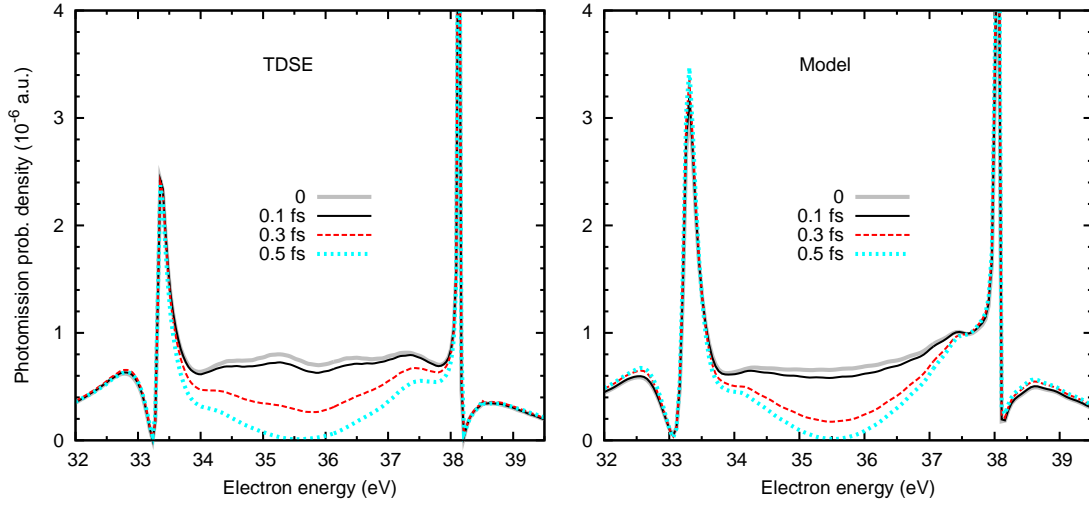


FIG. 8: PES for the s -wave with various time delays (t_0) calculated by TAE-TDSE and the present model. In both calculations, the signal in the middle between the two resonances attenuates dramatically along t_0 , and drops to nearly zero at $t_0 = 0.5$ where the XUV is on top of the zero laser field.

VII. CONCLUDING MARKS

We have reviewed the few-level model for the autoionizing wave packet excited by an XUV IAP and dressed by an intense dressing field. For the simplest case, the three-level model is described where the total wavefunction, including the broadband continuum components, is constructed. Taking the resonantly coupled $2s2p(^1P)$ and $2s^2(^1S)$ resonances in helium as an example, the PES and PAS are simulated, where the spectral features are manipulated by the intensity and time delay of the IR and analyzed by the Rabi oscillation between the resonances. By taking into account the propagation effect, with specific dressing field parameters, an emission peak of the XUV at the resonance energy can be stabilized in the medium in the millimeter distance scale, which demonstrates an ultrafast control over an attosecond pulse. In a more complex model where multiple resonances and the coupling with continuum states are considered, the calibration of the model by an *ab initio* calculation suggests that the continuum-continuum coupling has an essential contribution in the ultrafast XUV+IR scheme, especially at the beginning of the photoionization.

Attosecond light sources have renewed the interests in autoionizing systems, where certain recent experiments have been carried out beyond the scope of this review, such as the autoionization in molecular Rydberg states [45], the two-photon coupling between the AISs through an intermediate state [46], and continuous shift of the asymmetry of Fano resonances by an intense laser field [10]. With the rapid ongoing development, the demand for insightful and efficient models are expected to keep rising.

Acknowledgements

This work was supported in part by Chemical Sciences, Geosciences and biosciences Division, Office of Basic Energy Sciences, Office of Science, U. S. Department of Energy. T. M. Was supported by Grants-in-Aid for Scientific Research (A), (B), and (C) from the Ministry of Education, Culture, Sports, Science and Technology, Japan. W.-C. C. thanks G. Sansone for discussions on transient absorption spectroscopy, and T. Pfeifer and C. Ott for discussions on the continuum-continuum coupling of autoionizing states.

References

- [1] A. McPherson, G. Gibson, U. J. H. Jara, T. S. Luk, I. A. McIntyre, K. Boyer, and C. K. Rhodes, *J. Opt. Soc. Am. B* **4**, 595 (1987).
- [2] M. Ferray, A. L'Huillier, X. F. Li, L. A. Lompre, G. Mainfray, and C. Manus, *J. Phys. B: At. Mol. Opt. Phys.* **21**, L31 (1988).
- [3] J. M. Dahlström, Ph.D. thesis (2011).
- [4] A. S. Sandhu and X.-M. Tong, *IEEE J. Sel. Top. Quant. Electron.* **18**, 351 (2012).
- [5] M. Hentschel, R. Kienberger, C. Spielmann, G. A. Reider, N. Milosevic, T. Brabec, P. Corkum, U. Heinzmann, M. Drescher, and F. Krausz, *Nature* **414**, 509 (2001).
- [6] M. Uiberacker, T. Uphues, M. Schultze, A. J. Verhoef, V. Yakovlev, M. F. Kling, J. Rauschenberger, N. M. Kabachnik, H. Schröder, M. Lezius, et al., *Nature* **446**, 627 (2007).
- [7] H. Wang, M. Chini, S. Chen, C.-H. Zhang, F. He, Y. Cheng, Y. Wu, U. Thumm, and Z. Chang, *Phys. Rev. Lett.* **105**, 143002 (2010).
- [8] S. Gilbertson, M. Chini, X. Feng, S. Khan, Y. Wu, and Z. Chang, *Phys. Rev. Lett.* **105**, 263003 (2010).
- [9] E. Skantzakis, P. Tzallas, J. E. Kruse, C. Kalpouzos, O. Faucher, G. D. Tsakiris, and D. Charalambidis, *Phys. Rev. Lett.* **105**, 043902 (2010).
- [10] C. Ott, A. Kaldun, P. Raith, K. Meyer, M. Laux, J. Evers, C. H. Keitel, C. H. Greene, and T. Pfeifer, *Science* **340**, 716 (2013).
- [11] M. Chini, B. Zhao, H. Wang, Y. Cheng, S. X. Hu, and Z. Chang, *Phys. Rev. Lett.* **209**, 073601 (2012).
- [12] F. Kelkensberg, C. Lefebvre, W. Siu, O. Ghafur, T. T. Nguyen-Dang, O. Atabek, A. Keller, V. Serov, P. Johnsson, M. Swoboda, et al., *Phys. Rev. Lett.* **103**, 123005 (2009).
- [13] G. Sansone, F. Kelkensberg, J. F. Peérez-Torres, F. Morales, M. F. Kling, W. Siu, O. Ghafur, P. Johnsson, M. Swoboda, E. Benedetti, et al., *Nature* **465**, 763 (2010).
- [14] U. Fano, *Phys. Rev.* **124** (1961).
- [15] T. Brabec and F. Krausz, *Rev. Mod. Phys.* **72**, 545 (2000).
- [16] S. E. Harris, J. E. Field, and A. Imamoglu, *Phys. Rev. Lett.* **64**, 1107 (1990).
- [17] P. Lambropoulos and P. Zoller, *Phys. Rev. A* **24**, 379 (1981).
- [18] H. Bachau, P. Lambropoulos, and R. Shakeshaft, *Phys. Rev. A* **34**, 4785 (1986).
- [19] L. B. Madsen, P. Schlagheck, and P. Lambropoulos, *Phys. Rev. Lett.* **85**, 42 (2000).
- [20] S. I. Themelis, P. Lambropoulos, and M. Meyer, *J. Phys. B: At. Mol. Opt. Phys.* **37**, 4281 (2004).
- [21] N. E. Karapanagioti, O. Faucher, Y. L. Shao, D. Charalambidis, H. Bachau, and E. Cormier, *Phys. Rev. Lett.* **74**, 2431 (1995).
- [22] Z. H. Loh, C. H. Greene, and S. R. Leone, *Chem. Phys.* **350**, 7 (2008).

- [23] M. Fleischhauer, A. Imamoglu, and J. P. Marangos, *Rev. Mod. Phys.* **77**, 633 (2005).
- [24] T. Mercouris, Y. Komninos, and C. A. Nicolaides, *Phys. Rev. A* **75**, 013407 (2007).
- [25] W.-C. Chu and C. D. Lin, *Phys. Rev. A* **82**, 053415 (2010).
- [26] J. Itatani, F. Quéré, G. L. Yudin, M. Y. Ivanov, F. Krausz, and P. B. Corkum, *Phys. Rev. Lett.* **88**, 173903 (2002).
- [27] M. Kitzler, N. Milosevic, A. Scrinzi, F. Krausz, and T. Brabec, *Phys. Rev. Lett.* **88**, 173904 (2002).
- [28] E. Goulielmakis, M. Uiberacker, R. Kienberger, A. Baltuska, V. Yakovlev, A. Scrinzi, T. Westerwalbesloh, U. Kleineberg, U. Heinzmann, M. Drescher, et al., *Science* **305**, 1267 (2004).
- [29] M. Wickenhauser and J. Burgdörfer, *Laser Phys.* **14**, 492 (2004).
- [30] Z. X. Zhao and C. D. Lin, *Phys. Rev. A* **71**, 060702(R) (2005).
- [31] J. Zhao and M. Lein, *New J. Phys.* **14**, 065003 (2012).
- [32] L. Argenti, C. Ott, T. Pfeifer, and F. Martín, p. arXiv:1211.2566v1 (2012).
- [33] W.-C. Chu, S.-F. Zhao, and C. D. Lin, *Phys. Rev. A* **84**, 033426 (2011).
- [34] W.-C. Chu and C. D. Lin, *Phys. Rev. A* **85**, 013409 (2012).
- [35] W.-C. Chu and C. D. Lin, *J. Phys. B: At. Mol. Opt. Phys.* **45**, 201002 (2012).
- [36] W.-C. Chu and C. D. Lin, *Phys. Rev. A* **87**, 013415 (2013).
- [37] G. Alzetta, A. Gozzini, L. Moi, and G. Orriols, *Nuovo Cimento Soc. Ital. Fis. B* **36**, 5 (1976).
- [38] *Prog. Opt.* **35**, 257 (1996).
- [39] M. Holler, F. Schapper, L. Gallmann, and U. Keller, *Phys. Rev. Lett.* **106**, 123601 (2011).
- [40] M. B. Gaarde, C. Buth, J. L. Tate, and K. J. Schafer, *Phys. Rev. A* **83**, 013419 (2011).
- [41] S. H. Autler and C. H. Townes, *Phys. Rev.* **100**, 703 (1955).
- [42] A. Ishimaru, *Wave Propagation and Scattering in Random Media* (New York: IEEE, 1997), chap. 6.
- [43] A. Hishikawa, M. Fushitani, Y. Hikosaka, A. Matsuda, C.-N. Liu, T. Morishita, E. Shigemasa, M. Nagasono, K. Tono, T. Togashi, et al., *Phys. Rev. Lett.* **107**, 243003 (2011).
- [44] C. N. Liu, A. Hishikawa, and T. Morishita, *Phys. Rev. A* **86**, 053426 (2012).
- [45] H. Timmers, N. Shivaram, and A. Sandhu, *Phys. Rev. Lett.* **109**, 173001 (2012).
- [46] C. Ott, A. Kaldun, P. Raith, K. Meyer, M. Laux, Y. Zhang, S. Hagstotz, T. Ding, R. Heck, and T. Pfeifer, arXiv:1205.0519v1 (2012).